GSC Biological and Pharmaceutical Sciences
eISSN: 2581-3250 CODEN (USA): GBPSC2
Cross Ref DOI: 10.30574/gscbps
Journal homepage: https://gsconlinepress.com/journals/gscbps/

(RESEARCH ARTICLE)

Check for updates

Comparative binding mechanisms of the reference inhibitor BIBR1532 and the *Andrographis paniculata* candidate LTS0004521 against telomerase

Tuan Thanh Nguyen and Quan Ke Thai *

Faculty of Natural science education, Saigon University, 273 An Duong Vuong, Cho Quan ward, Ho Chi Minh City, Vietnam, 700000.

GSC Biological and Pharmaceutical Sciences, 2026, 35(02), 121-133

Publication history: Received on 27 March 2026; revised on 09 May 2026; accepted on 11 May 2026

Article DOI: https://doi.org/10.30574/gscbps.2026.35.2.0182

Abstract

Telomerase is a critical therapeutic target in cancer, and understanding the molecular basis of ligand binding is essential for the rational design of effective inhibitors. In this study, we employed molecular dynamics simulations combined with interaction profiling and MM/GBSA energy decomposition to investigate and compare the binding mechanisms of the reference inhibitor BIBR1532 and the candidate compound LTS0004521 of *Andrographis paniculata*. Trajectory analysis revealed that both ligands maintained stable binding within the active site; however, they exhibited fundamentally distinct interaction patterns. BIBR1532 formed a compact and interaction-dense binding mode, dominated by strong electrostatic anchoring involving key residues such as ARG486 and ARG69, supported by persistent hydrophobic contacts. In contrast, LTS0004521 displayed a more dynamic and distributed interaction network, characterized by reduced electrostatic contributions and extensive hydrogen bonding with multiple residues, including VAL491, TYR551, GLY553, and LEU554. Per-residue energy decomposition further highlighted these differences, with BIBR1532 showing large electrostatic contributions offset by polar solvation penalties, whereas LTS0004521 exhibited a more balanced energetic profile driven by van der Waals and polar interactions across a broader residue set. Structural mapping of ligand–protein interactions confirmed that these distinct interaction strategies arise from differences in molecular architecture. Collectively, our results demonstrate that while BIBR1532 relies on localized anchoring, LTS0004521 achieves stabilization through an expanded interaction network. This shift in binding paradigm underscores the importance of interaction diversity in ligand design and provides valuable insights for the development of next-generation telomerase inhibitors with improved stability and adaptability.

Keywords: *Andrographis paniculata;* Andrographolide Derivatives; Telomerase; Cancer; Protein-Ligand Interaction; Molecular Dynamic Simulation.

1. Introduction

Cancer is characterized by uncontrolled cell proliferation and the acquisition of replicative immortality, a hallmark that is strongly associated with the maintenance of telomere length [1]. Telomerase, a ribonucleoprotein enzyme complex composed of a catalytic subunit (TERT) and an RNA template (TERC), plays a central role in this process by elongating telomeric DNA and preserving chromosomal integrity [1], [2]. While telomerase is inactive in most somatic cells, it is reactivated in approximately 85–90% of human cancers, enabling continuous cell division and tumor progression [3], [4], [5], [6], [7]. This widespread reactivation, coupled with its limited expression in normal tissues, makes telomerase an attractive and selective target for anticancer therapy.

Among small-molecule telomerase inhibitors, BIBR1532 has emerged as a prototypical non-nucleosidic inhibitor that directly targets the catalytic activity of telomerase [8]. It acts through noncompetitive inhibition at the hTERT active or allosteric site, leading to progressive telomere shortening and induction of cellular senescence and apoptosis [9], [10],

* Corresponding author: Quan Ke Thai

[11]. Despite its selectivity and well-characterized mechanism, BIBR1532 exhibits limitations, including moderate potency and reduced efficacy in certain tumor types, which has motivated the development of structurally optimized derivatives [12], [13], [14], [15]. Structure–activity relationship studies further indicate that its activity is closely linked to specific interaction motifs, including hydrophobic centers and charged functional groups, highlighting the importance of precise ligand–protein interactions in telomerase inhibition [16], [17], [18].

Natural products represent a rich source of structurally diverse bioactive compounds for anticancer drug discovery. In particular, *Andrographis paniculata* has attracted considerable attention due to its diterpenoid lactone constituents, especially andrographolide, which exhibit broad pharmacological activities including anticancer, anti-inflammatory, and immunomodulatory effects [19], [20]. Structural modification of andrographolide has been shown to enhance its bioactivity and target specificity, making its derivatives promising candidates for further development as anticancer agents [21], [22], [23]. Importantly, natural-product-derived scaffolds often provide flexible interaction capabilities, which may be advantageous when targeting dynamic enzymes such as telomerase [24], [25], [26].

In recent years, *in silico* approaches have become indispensable in early-stage drug discovery. Structure-based virtual screening, molecular docking, and molecular dynamics simulations (MDS) enable rapid identification and evaluation of potential telomerase inhibitors at atomic resolution [27]. In particular, MDS provides dynamic insights into ligand binding, allowing the characterization of conformational flexibility, interaction stability, and time-dependent behavior of telomerase–ligand complexes [28]. Beyond static binding affinity, increasing evidence suggests that the detailed analysis of interaction networks is critical for rational drug design [29], [30], [31]. Molecular dynamics studies have shown that ligands typically engage in multiple types of interactions—including hydrogen bonds, hydrophobic contacts, and ionic interactions—that collectively determine binding stability and specificity [32], [33], [34]. Moreover, recent studies emphasize that relying on a limited number of hotspot residues may render ligands vulnerable to conformational fluctuations or mutations, whereas ligands that form distributed and redundant interaction networks across multiple residues exhibit enhanced robustness and adaptability [35], [36], [37]. Such interaction diversity is particularly important for targets like telomerase, which undergo dynamic structural rearrangements during their catalytic cycle.

In a previous study, we applied a virtual screening strategy to compounds derived from *A. paniculata*, integrating molecular docking with molecular dynamics simulations [38]. This approach identified an andrographolide derivative (LOTUS accession: LTS0004521) exhibiting a higher binding affinity than the reference inhibitor BIBR1532 for the telomerase active site, with a well-defined binding orientation [38]. Building on these findings, the present study aims to elucidate the binding mechanisms of both BIBR1532 and the candidate compound through post–molecular dynamics analyses and detailed interaction profiling. By combining trajectory-based interaction mapping with binding free energy decomposition, we seek to characterize the molecular determinants underpinning binding stability and to underscore the importance of distributed interaction networks in the rational design of next-generation telomerase inhibitors.

2. Materials and methods

2.1. Extraction and preprocessing of molecular dynamics trajectories

In our previous study [38], molecular docking was performed to position BIBR1532 and LTS0004521 within the active site of telomerase. The resulting protein–ligand complexes were subsequently subjected to 200 ns molecular dynamics simulations using GROMACS [39]. Visual inspection of the trajectories using Visual Molecular Dynamics (VMD) [40] confirmed that both ligands remained stably bound within the binding pocket throughout the simulation. For subsequent analyses, the 100 ns of each trajectory, corresponding to the equilibrated phase, were extracted [38]. A total of 10,000 evenly spaced frames were generated from this interval to ensure adequate sampling of conformational space. Each frame was converted into Protein Data Bank (.pdb) format using VMD [40], enabling compatibility with downstream structural and interaction analysis tools.

2.2. Automated protein–ligand interaction profiling

To systematically characterize protein–ligand interactions across the trajectory, we developed an automated workflow implemented in Python, integrating the Protein–Ligand Interaction Profiler (PLIP) [41]. For each extracted frame, PLIP was used to identify and classify interaction types, including: (i) hydrophobic interactions, (ii) hydrogen bonds, (iii) π–π stacking interactions, (iv) π–cation interactions, and (v) salt bridges. All interaction detection parameters were maintained at their default PLIP settings to ensure methodological consistency. Briefly, hydrogen bonds were identified based on a donor–acceptor distance cutoff of ≤ 3.5 Å and a minimum donor–hydrogen–acceptor angle of 120°.

Hydrophobic interactions were defined by contacts between nonpolar atoms within a distance threshold of 4.0 Å. π–π stacking interactions were detected when aromatic ring centroids were within 5.5 Å and exhibited appropriate angular orientation. π–cation interactions were identified based on proximity (≤ 6.0 Å) between a positively charged group and an aromatic ring system. Salt bridges were defined by interactions between oppositely charged groups within a cutoff distance of 4.0 Å.

2.3. Data processing and statistical analysis

The interaction data generated by PLIP for each frame were parsed and aggregated using Python-based libraries. Interaction frequencies were calculated as the percentage of frames in which a given residue participated in a specific interaction type. Temporal profiles of total interaction counts were also derived to assess fluctuations in ligand binding over time. To improve interpretability of time-dependent interaction data, smoothing techniques such as rolling averages were applied where appropriate. Summary statistics, including mean values and standard deviations or standard errors, were computed across the full trajectory dataset.

2.4. Visualization of interaction patterns

Interaction data were visualized using Python-based libraries to generate heatmaps, line plots, and residue-level interaction profiles. Two-dimensional interaction diagrams were constructed to illustrate key ligand–protein contacts and their structural context. Three-dimensional representations of binding modes were generated using UCSF Chimera [42] and PyMOL, enabling detailed visualization of ligand orientation and interaction geometry within the telomerase active site.

2.5. Binding free energy decomposition analysis

Binding free energy calculations were performed using the Molecular Mechanics/Generalized Born Surface Area (MM/GBSA) method as implemented in the gmx_MMPBSA tool [43]. The binding free energy ($\Delta G_{MM/GBSA}$) for each protein–ligand complex was estimated according to the following equation::

$$\Delta G_{MM/GBSA} = \Delta G_{Complex} - \Delta G_{Protein} - \Delta G_{ligand} \quad (1)$$

To obtain residue-level insights, per-residue free energy decomposition was conducted, allowing the contribution of individual amino acids to ligand binding to be quantified. The total binding free energy was decomposed into distinct energetic components as follows::

$$\Delta G = \Delta G_{vdW} + \Delta G_{Eletrostatic} + \Delta G_{GB} + \Delta G_{Non-polar} \quad (2)$$

here, $G_{Eletrostatic}$, and ΔG_{vdW} represent the van der Waals and electrostatic interaction energies between the protein and ligand, respectively. ΔG_{GB} corresponds to the polar solvation free energy estimated using the Generalized Born model, while $\Delta G_{Non-polar}$ represents the non-polar contribution to solvation, typically associated with solvent-accessible surface area. All calculations were performed using snapshots extracted from the equilibrated portion of the MDS trajectories. The resulting energy components were averaged over the sampled frames and reported as mean ± standard error of the mean (SEM), providing a quantitative measure of the stability and variability of residue-level contributions.

3. Results

In molecular dynamics simulations, rigorous assessment of equilibration and convergence is critical to ensure the reliability and statistical validity of the results, as only properly equilibrated and sufficiently sampled trajectories can support accurate downstream analyses [44], [45], [46]. Based on 200 ns simulation of our previous research [38], we confirmed that the last 100 ns of the LTS0004521 simulation reached simulated equilibrium, and this corresponds to the reference molecule BIBR1532. Thus, 10,000 frames from the last 100 ns of each system's simulation were collected for further analysis. The interaction dynamics of BIBR1532 within the binding pocket remained stable over the 10,000-frame molecular dynamics trajectory (Figure 1A). The total number of contacts fluctuated between 3 and 14, with an average of 7.8 ± 1.7 (Figure 1A), indicating a moderately dense but persistent interaction network. Temporal smoothing revealed that, despite short-timescale fluctuations, the interaction profile remained consistently centered around the mean, with no evidence of ligand dissociation. A subtle increase in interaction density was observed between 8,500 and 9,500 frames, suggestive of a transiently enhanced binding state (Figure 1A). Residue-level analysis revealed a structured yet dynamic interaction pattern. ARG486 emerged as the dominant contributor, maintaining persistent and

high-frequency contacts throughout the trajectory, consistent with a central role in anchoring BIBR1532 (Figure 1B). PHE494 also displayed sustained interactions, albeit at lower intensity, likely contributing to ligand stabilization through hydrophobic or π-mediated contacts. ILE550, ILE497, and VAL491 exhibited moderate and fluctuating interaction frequencies, indicative of a flexible hydrophobic environment that accommodates ligand motion (Figure 1B). ARG69 showed a markedly intermittent interaction profile, characterized by sporadic high-contact events separated by extended inactive periods, suggesting a conditional or transient stabilizing role (Figure 1B). TYR551 contributed minimally overall but displayed localized increases in interaction frequency during the later stages of the simulation (Figure 1B). These findings indicate that BIBR1532 binding is governed by a core set of persistent interactions, primarily involving ARG486 and PHE494, embedded within a dynamically adaptive interaction network. This balance between stability and flexibility likely underpins the sustained binding of BIBR1532 while permitting conformational fluctuations within the binding site.

The interaction profile of LTS0004521 exhibited a comparable overall stability to that observed for BIBR1532, with the total number of contacts fluctuating between 3 and 14 and an average of 8.0 ± 1.7 over the 10,000-frame trajectory (Figure 1B). Residue-level mapping highlighted a distinct interaction pattern compared to BIBR1532. VAL491 and PHE494 emerged as consistently engaged residues, maintaining relatively uniform interaction frequencies across the trajectory and likely forming a hydrophobic core that stabilizes LTS0004521. TYR551 and LEU554 also contributed sustained, moderate interactions, supporting ligand accommodation within the binding pocket. In contrast, ARG486 displayed a markedly reduced and transient interaction profile. Strong contacts were observed primarily during the early phase of the simulation (0–1,200 frames), after which interactions diminished substantially and remained sporadic. This contrasts with its persistent role in BIBR1532 binding, suggesting a different anchoring mechanism for LTS0004521. Similarly, ILE497 exhibited phase-dependent interactions, with increased contact frequency during the mid-trajectory interval (2,000–6,000 frames), coinciding with the observed fluctuation in total interaction count. ILE550 contributed minimally throughout most of the simulation, with only minor increases toward the terminal frames. Collectively, these results indicate that LTS0004521 binding is governed by a more dynamic and redistributed interaction network, relying less on strong, persistent electrostatic anchoring and more on hydrophobic and transient contacts involving residues such as VAL491, PHE494, and LEU554. The observed mid-trajectory destabilization and subsequent recovery further suggest conformational adaptability of the ligand within the binding site, potentially reflecting multiple binding substates.

The interaction type analysis (Table 1) revealed marked differences in the binding mechanisms of BIBR1532 and LTS0004521, despite partial overlap in key residues. BIBR1532 binding was dominated by a combination of persistent hydrophobic contacts and strong electrostatic interactions centered on ARG486. This residue exhibited high interaction occupancies across multiple interaction types, including hydrophobic contacts (94.4%), hydrogen bonds (62.5%), π-cation interactions (18.2%), and salt bridges (58.2%), highlighting its role as a primary anchoring point. In addition, ARG69 contributed substantially through salt bridge formation (45.9%), further reinforcing electrostatic stabilization. Hydrophobic interactions with PHE494 (94.1%), ILE550 (79.9%), VAL491 (64.5%), and ILE497 (63.1%) formed a stable nonpolar environment surrounding the ligand, while TYR551 and LEU485 contributed more modestly. In contrast, LTS0004521 displayed a distinct interaction profile characterized by reduced electrostatic contributions and a greater reliance on hydrogen bonding and redistributed hydrophobic contacts. Notably, ARG486 showed a significant decrease in interaction occupancy across all interaction types, with hydrophobic interactions reduced to 29.9% and salt bridges to 12.8%, and a complete loss of hydrogen bond and π-cation contributions. Similarly, ARG69 no longer participated in salt bridge formation, indicating the absence of strong ionic anchoring. Instead, LTS0004521 formed extensive hydrogen bond networks involving multiple residues. VAL491 (98.3%), GLY553 (92.4%), TYR551 (79.8%), and LEU554 (76.7%) exhibited high hydrogen bond occupancies, suggesting a shift toward polar stabilization within the binding pocket. Hydrophobic interactions remained relevant but were redistributed, with strong contributions from PHE494 (84.7%), LEU485 (78.7%), and ILE497 (41.3%), while interactions with ILE550 were minimal (2.3%). Collectively, these findings indicate that BIBR1532 binding is driven by a synergistic combination of hydrophobic packing and strong electrostatic anchoring, particularly involving ARG486 and ARG69. LTS0004521 adopts a more flexible binding mode, characterized by diminished ionic interactions and an expanded hydrogen bond network distributed across multiple residues. This shift in interaction strategy is consistent with the more dynamic interaction patterns observed in the trajectory analysis and suggests fundamentally different stabilization mechanisms within the same binding site.

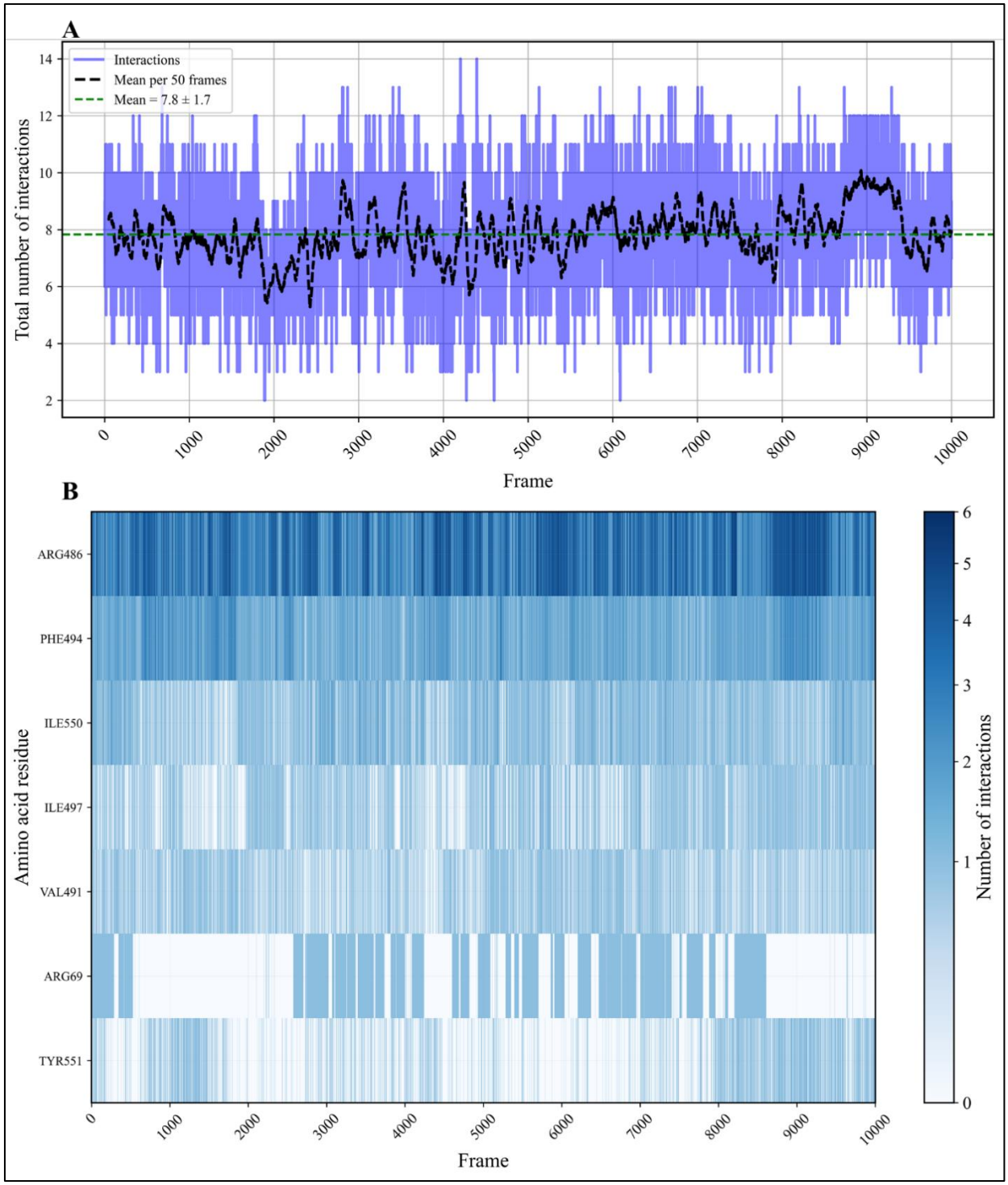

Figure 1 Interaction analysis of BIBR1532 within the telomerase binding pocket in the molecular dynamics trajectory. ***(A)*** *Temporal evolution of the total number of protein–ligand interactions per frame, illustrating the stability and fluctuation of the interaction network throughout the simulation. Each data point represents the total number of interactions identified in an individual frame, providing insight into the dynamic behavior of BIBR1532 binding.* ***(B)*** *Residue-level interaction mapping showing the frequency and persistence of amino acid residues involved in interactions with BIBR1532 across the trajectory. The color scale reflects interaction frequency, enabling identification of key residues contributing to ligand stabilization*

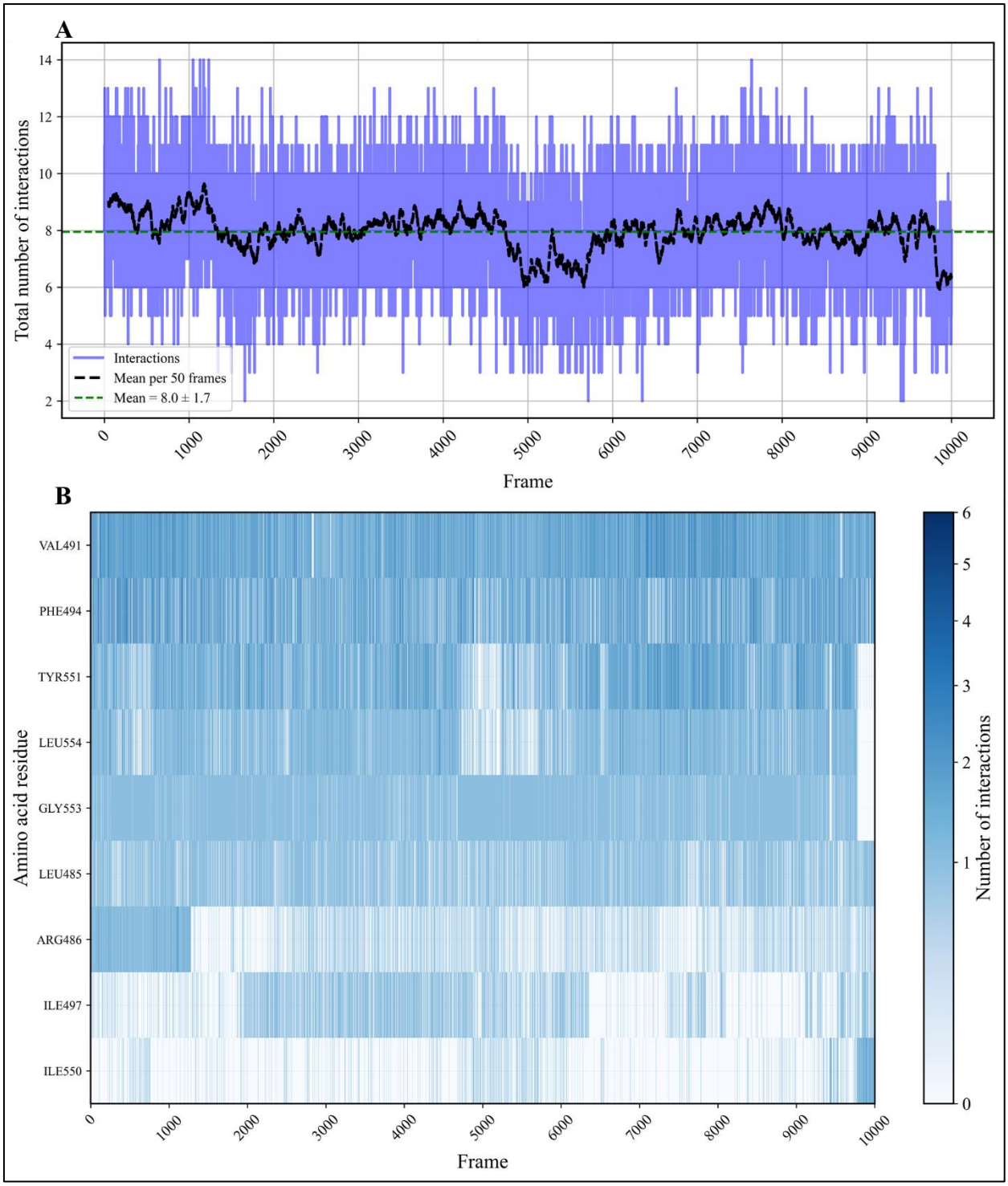

Figure 2 Interaction analysis of LTS0004521 in complex with telomerase during molecular dynamics simulation. (A) Time-resolved profile of the total number of protein–ligand interactions per frame, highlighting fluctuations and transient changes in binding stability over the course of the simulation; (B) Residue-wise interaction frequency map illustrating the distribution and persistence of interactions formed between LTS0004521 and telomerase residues. This representation enables comparison of interaction patterns and identification of dominant and transient binding contributors

Table 1 Interaction frequency (%) of telomerase residues with BIBR1532 and LTS0004521 across the MDS trajectory.

		Hydrophobic Interactions	**Hydrogen Bonds**	**π-Cation Interactions**	**Salt Bridges**
ARG69	BIBR1532	-	-	-	45.9%
	LTS0004521	-	-	-	-
ARG486	BIBR1532	94.4%	62.5%	18.2%	58.2%
	LTS0004521	29.9%	-	-	12.8%
PHE494	BIBR1532	94.1%	-	-	-
	LTS0004521	84.7%	-	-	-
ILE550	BIBR1532	79.9%	-	-	-
	LTS0004521	2.3%	12.8%	-	-
ILE497	BIBR1532	63.1%	-	-	-
	LTS0004521	41.3%	-	-	-
VAL491	BIBR1532	64.5%	-	-	-
	LTS0004521	50.1%	98.3%	-	-
TYR551	BIBR1532	34.4%	-	-	-
	LTS0004521	42.5%	79.8%	-	-
LEU554	BIBR1532	-	-	-	-
	LTS0004521	16.7%	76.7%	-	-
GLY553	BIBR1532	-	-	-	-
	LTS0004521	-	92.4%	-	-
LEU485	BIBR1532	10.8%	-	-	-
	LTS0004521	78.7%	-	-	-

The 2D interaction mapping further substantiated the distinct binding modes inferred from the interaction frequency analysis (Table 1), by linking specific interaction types to the structural features of BIBR1532 and LTS0004521 (Figure 3A and B). For BIBR1532 (Figure 3A), the interaction pattern was spatially organized around a central amide-linked scaffold connecting aromatic moieties. The positively charged nitrogen within the amide region served as a key interaction hub, consistent with the high occupancy of electrostatic interactions observed for ARG486. The presence of both hydrogen bonding and π-cation interactions in this region aligns with the multifunctional role of ARG486 identified in Table 1. In addition, the terminal carboxyl group contributed to salt bridge formation, supporting the substantial involvement of ARG69. The extended aromatic systems of BIBR1532 provided a structural basis for its strong hydrophobic contacts with residues such as PHE494, ILE550, and VAL491, enabling stable packing within the binding pocket. Collectively, the relatively rigid and planar architecture of BIBR1532 facilitates simultaneous engagement in hydrophobic and electrostatic interactions, reinforcing its role as a tightly anchored ligand. In contrast, LTS0004521 (Figure 3B) displayed a markedly different interaction topology, consistent with its interaction profile in Table 1. The structure is characterized by a bulky, polycyclic framework with multiple hydroxyl groups, which serve as sites for hydrogen bond formation. These polar functionalities are spatially distributed across the molecule, enabling simultaneous interactions with multiple residues, in agreement with the high hydrogen bond occupancies observed for VAL491, GLY553, TYR551, and LEU554. Unlike BIBR1532, LTS0004521 lacks a well-defined charged center capable of sustaining persistent salt bridges, explaining the diminished contribution of ARG69 and ARG486. Furthermore, the hydrophobic interactions of LTS0004521 are more diffusely distributed across its scaffold, rather than concentrated in a single aromatic core. This structural feature supports its interaction with residues such as PHE494 and LEU485, while also contributing to the dynamic and adaptable binding mode observed during the trajectory analysis. The combination of a flexible hydrophobic surface and multiple hydrogen bond donors results in a binding mechanism that is less dependent on strong electrostatic anchoring and more reliant on distributed polar interactions. Together, the structural

mapping highlights a fundamental distinction between the two ligands: BIBR1532 achieves stable binding through a compact, interaction-dense architecture centered on key charged residues, whereas LTS0004521 adopts a more flexible and distributed interaction strategy driven by extensive hydrogen bonding. These observations are fully consistent with the interaction occupancy data and dynamic behavior described above, reinforcing the mechanistic divergence in their binding modes.

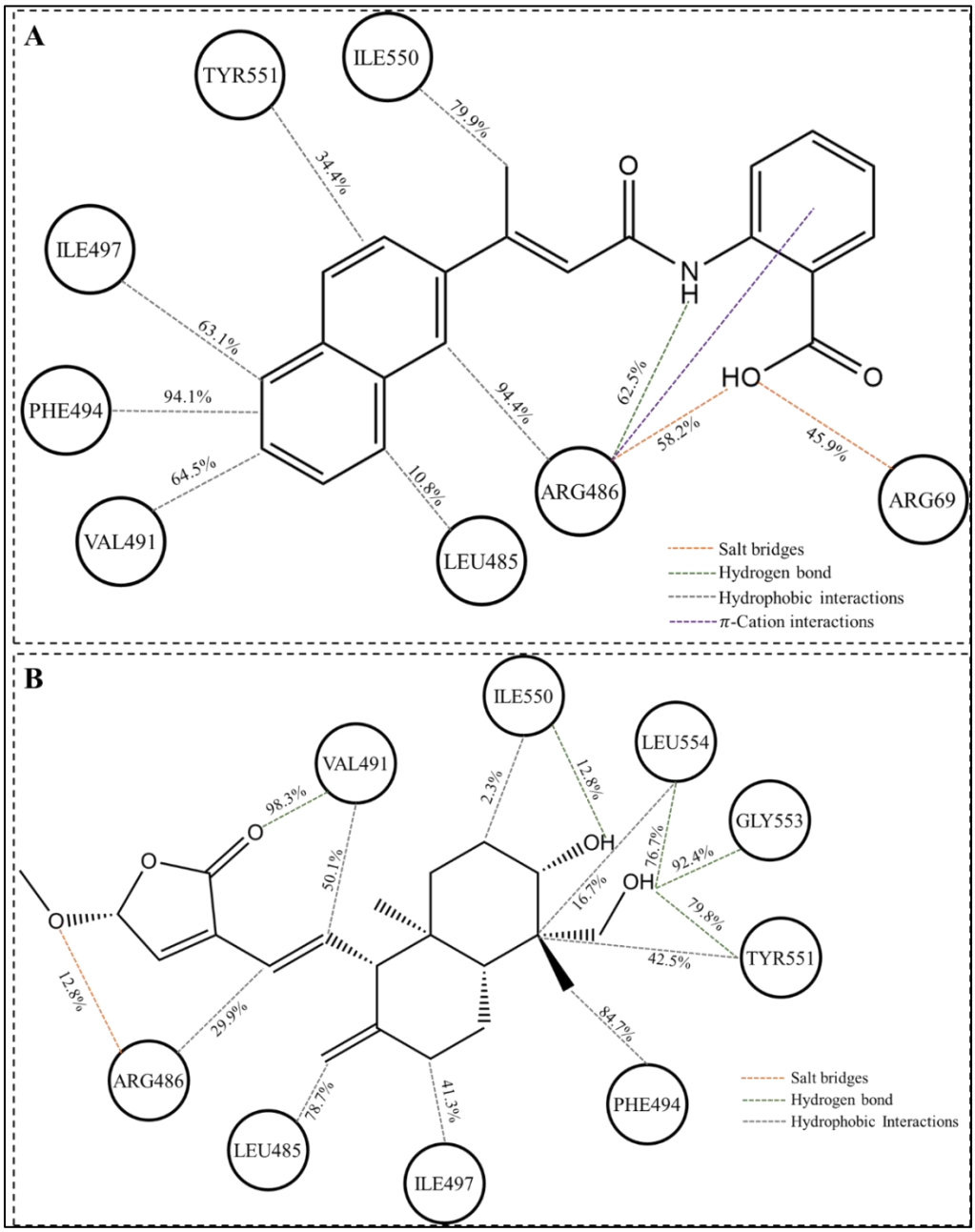

Figure 3 Two-dimensional interaction profiles of ligand binding within the telomerase active site.

Per-residue MM/GBSA decomposition (Table 2) revealed distinct energetic signatures underlying the binding of BIBR1532 and LTS0004521, consistent with the interaction patterns described above. For BIBR1532, binding was dominated by strong electrostatic contributions from key charged residues. ARG486 emerged as the principal energetic contributor, with a highly favorable total binding energy (−8.554 ± 0.227 kcal·mol^{-1}), primarily driven by a large electrostatic term (−71.981 ± 0.172 kcal·mol^{-1}) that was partially offset by polar solvation penalties. Similarly, ARG69 contributed significantly (−3.689 ± 0.294 kcal·mol^{-1}), again reflecting strong electrostatic stabilization balanced by desolvation effects. These findings are fully consistent with the high occupancy of salt bridges and hydrogen bonds observed for these residues in Table 1. Hydrophobic residues also contributed favorably, albeit to a lesser extent. ILE550 (−1.163 ± 0.054 kcal·mol^{-1}), PHE494 (−0.792 ± 0.058 kcal·mol^{-1}), and VAL491 (−0.297 ± 0.055 kcal·mol^{-1}) showed

stabilizing van der Waals interactions, supporting the role of a compact hydrophobic environment in ligand binding. Other residues, including TYR551, ILE497, GLY553, and LEU485, exhibited only minor energetic contributions, indicating a secondary or supportive role. Overall, the energetic landscape of BIBR1532 binding is characterized by strong electrostatic anchoring complemented by hydrophobic stabilization.

In contrast, LTS0004521 displayed a markedly different energy distribution, with reduced electrostatic contributions and a broader involvement of multiple residues through moderate van der Waals interactions. Notably, ARG486 showed a substantial decrease in total binding energy (−1.595 ± 0.315 kcal·mol^{-1}), with the electrostatic term becoming negligible, consistent with the loss of persistent ionic interactions observed in Table 1. ARG69 contributed negligibly (0.026 ± 0.241 kcal·mol^{-1}), further confirming the absence of electrostatic anchoring. Instead, binding of LTS0004521 was driven by a combination of hydrophobic and distributed polar interactions across several residues. PHE494 (−2.785 ± 0.056 kcal·mol^{-1}) and VAL491 (−2.363 ± 0.049 kcal·mol^{-1}) emerged as major contributors, dominated by favorable van der Waals interactions. TYR551 (−1.750 ± 0.067 kcal·mol^{-1}), LEU554 (−1.934 ± 0.047 kcal·mol^{-1}), and LEU485 (−1.006 ± 0.049 kcal·mol^{-1}) also contributed substantially, reflecting a broader distribution of stabilizing interactions. Additionally, GLY553 (−0.953 ± 0.046 kcal·mol^{-1}) showed notable contribution, consistent with its high hydrogen bond occupancy. Across residues, polar solvation penalties were generally lower in magnitude compared to BIBR1532, reflecting the reduced role of strong electrostatic interactions and the greater reliance on balanced polar and nonpolar contributions. Taken together, these results demonstrate that BIBR1532 binding is energetically dominated by a small number of residues with strong electrostatic contributions, particularly ARG486 and ARG69, whereas LTS0004521 achieves stabilization through a more evenly distributed network of moderate interactions, primarily driven by van der Waals and hydrogen bonding contributions. This energetic redistribution aligns closely with the interaction frequency data and structural mapping, reinforcing the fundamentally different binding strategies of the two ligands.

Table 2 Per-residue binding free energy decomposition (kcal·mol^{-1}) calculated using the MM/GBSA approach.

Residue	Compound	van der Waals	Electrostatic	Polar Solvation	Non-Polar Solvation	Total
ARG69	BIBR1532	0.484 ± 0.021	-54.761 ± 0.218	50.768 ± 0.188	-0.179 ± 0.002	-3.689 ± 0.294
	LTS0004521	-0.008 ± 0.022	0.741 ± 0.173	-0.707 ± 0.156	-0.001 ± 0.002	0.026 ± 0.241
ARG486	BIBR1532	-2.765 ± 0.023	-71.981 ± 0.172	66.764 ± 0.135	-0.572 ± 0.001	-8.554 ± 0.227
	LTS0004521	-2.237 ± 0.021	0.853 ± 0.230	0.182 ± 0.207	-0.394 ± 0.002	-1.595 ± 0.315
PHE494	BIBR1532	-1.359 ± 0.027	-0.626 ± 0.026	1.367 ± 0.016	-0.173 ± 0.001	-0.792 ± 0.058
	LTS0004521	-2.683 ± 0.024	-0.207 ± 0.023	0.516 ± 0.014	-0.412 ± 0.002	-2.785 ± 0.056
ILE550	BIBR1532	-1.451 ± 0.020	0.847 ± 0.023	-0.249 ± 0.021	-0.311 ± 0.002	-1.163 ± 0.054
	LTS0004521	-0.700 ± 0.019	-0.089 ± 0.025	0.460 ± 0.022	-0.119 ± 0.002	-0.447 ± 0.055
ILE497	BIBR1532	-0.354 ± 0.020	-0.698 ± 0.015	0.819 ± 0.009	-0.020 ± 0.000	-0.253 ± 0.045
	LTS0004521	-0.617 ± 0.020	0.061 ± 0.017	-0.002 ± 0.010	-0.059 ± 0.000	-0.617 ± 0.050
VAL491	BIBR1532	-0.983 ± 0.017	3.768 ± 0.029	-3.024 ± 0.020	-0.058 ± 0.001	-0.297 ± 0.055
	LTS0004521	-1.646 ± 0.016	-1.053 ± 0.022	0.542 ± 0.021	-0.206 ± 0.001	-2.363 ± 0.049
TYR551	BIBR1532	-0.823 ± 0.027	0.363 ± 0.035	0.308 ± 0.014	-0.038 ± 0.000	-0.190 ± 0.064
	LTS0004521	-1.698 ± 0.027	-0.271 ± 0.041	0.344 ± 0.015	-0.125 ± 0.000	-1.750 ± 0.067
LEU554	BIBR1532	-0.087 ± 0.017	-0.942 ± 0.017	1.031 ± 0.010	0.000 ± 0.000	0.002 ± 0.045
	LTS0004521	-1.181 ± 0.016	-1.369 ± 0.019	0.747 ± 0.010	-0.131 ± 0.001	-1.934 ± 0.047
GLY553	BIBR1532	-0.036 ± 0.011	-1.233 ± 0.030	1.215 ± 0.018	0.000 ± 0.001	-0.055 ± 0.044
	LTS0004521	-0.504 ± 0.011	-1.663 ± 0.032	1.357 ± 0.019	-0.143 ± 0.001	-0.953 ± 0.046
LEU485	BIBR1532	-0.402 ± 0.017	0.468 ± 0.019	-0.618 ± 0.009	-0.010 ± 0.000	-0.563 ± 0.047
	LTS0004521	-1.080 ± 0.017	-0.417 ± 0.021	0.549 ± 0.012	-0.059 ± 0.000	-1.006 ± 0.049

4. Discussion

Understanding the molecular basis of ligand–protein interactions through molecular dynamics simulations has become essential for rational drug design, particularly for complex targets such as telomerase. Detailed characterization of interaction networks—beyond static docking poses—provides critical insights into binding stability, specificity, and adaptability under dynamic physiological conditions. Previous studies have emphasized that dynamic interaction profiling, including hydrogen bonding persistence, hydrophobic contacts, and energetic decomposition, offers a more realistic representation of ligand behavior than single-point structural analyses [47], [48], [49].

In the present study, BIBR1532 exhibited a binding mode strongly dependent on a limited number of key residues, particularly ARG486 and ARG69. These residues contributed substantial electrostatic stabilization through salt bridges and hydrogen bonding, as supported by both interaction frequency and MM/GBSA energy decomposition. Such anchoring mechanisms are consistent with earlier reports describing BIBR1532 as a non-nucleosidic telomerase inhibitor that binds through specific electrostatic interactions within the active site [8], [15]. However, while strong anchoring can enhance binding affinity, it may also reduce adaptability, making the ligand more sensitive to local conformational fluctuations or mutations at critical residues. In contrast, LTS0004521 demonstrated a markedly different binding strategy characterized by a broader and more distributed interaction network. Instead of relying on dominant electrostatic anchors, this compound formed extensive hydrogen bond networks and hydrophobic contacts across multiple residues, including VAL491, TYR551, GLY553, and LEU554. This shift toward interaction redundancy and distribution is increasingly recognized as a desirable feature in ligand design, as it enhances binding resilience and reduces dependence on any single residue [50].

The energetic analysis further reinforced this distinction. While BIBR1532 binding was dominated by large electrostatic contributions offset by polar solvation penalties, LTS0004521 exhibited a more balanced energy profile, with moderate van der Waals and polar contributions distributed across multiple residues. Such energetic dispersion has been associated with improved ligand flexibility and adaptability within dynamic binding pockets, particularly for proteins like telomerase that undergo conformational rearrangements during function [51]. Importantly, the concept of expanding the interaction network—rather than relying on one or two anchoring residues—has significant implications for targeting telomerase. Telomerase is a highly dynamic ribonucleoprotein complex, and its active site environment is not rigid. Ligands that engage multiple residues through diverse interaction types are more likely to maintain stable binding across conformational states and may exhibit improved resistance to resistance-conferring mutations. This principle aligns with modern drug design strategies that favor interaction network optimization over hotspot dependence [52], [53], [54]. Our results suggest that while BIBR1532 achieves strong binding through focused electrostatic anchoring, LTS0004521 represents a more flexible and potentially robust binding paradigm by distributing interactions across a wider residue network. This distinction highlights the importance of comprehensive interaction analysis in MDS and supports the strategy of designing telomerase inhibitors that maximize interaction diversity to enhance stability, adaptability, and potentially therapeutic efficacy.

Despite providing detailed insights into the interaction mechanisms of BIBR1532 and LTS0004521, this study has several limitations that should be considered. Our analysis is based on a single simulation timescale, which, although sufficient to capture general stability and interaction trends, may not fully represent long-timescale conformational transitions of telomerase. Given the highly dynamic nature of this enzyme, extended simulations or enhanced sampling methods would be necessary to comprehensively explore alternative binding substates and rare events. MM/GBSA approach, while widely used for estimating binding free energies, relies on implicit solvent models and approximations that may not fully capture entropic contributions and long-range solvent effects. As a result, the absolute energy values should be interpreted with caution, and the conclusions are more robust in a comparative rather than quantitative sense. Interaction analysis focuses primarily on protein–ligand contacts and does not explicitly account for the role of RNA components or cofactors within the telomerase holoenzyme. Since telomerase function depends on a ribonucleoprotein complex, neglecting these elements may limit the physiological relevance of the binding modes observed. Finally, biochemical assays, mutagenesis studies, or cellular validation would be required to confirm whether the enhanced interaction network of LTS0004521 translates into improved inhibitory activity or resistance profiles.

5. Conclusion

This study provides a comprehensive molecular-level comparison of ligand binding mechanisms to telomerase through molecular dynamics simulations, interaction profiling, and MM/GBSA energy decomposition. BIBR1532 exhibits a binding mode dominated by strong, localized electrostatic anchoring, primarily involving key residues such as ARG486 and ARG69. In contrast, LTS0004521 adopts a more distributed interaction strategy, characterized by an expanded

network of hydrogen bonds and hydrophobic contacts across multiple residues. These findings highlight the importance of moving beyond single-residue anchoring toward the optimization of broader interaction networks in ligand design. Such an approach may enhance binding stability, adaptability, and robustness against conformational fluctuations within dynamic targets like telomerase. Overall, this work underscores the value of detailed interaction analysis in MDS as a framework for guiding the rational development of next-generation telomerase inhibitors.

Compliance with ethical standards

Disclosure of conflict of interest

No conflict of interest to be disclosed.

References

[1] S. E. Artandi and R. A. DePinho, "Telomeres and telomerase in cancer," (in eng), *Carcinogenesis,* vol. 31, no. 1, pp. 9-18, Jan 2010.

[2] B. Fernández-Varas *et al.*, "Clinical mutations in the TERT and TERC genes coding for telomerase components induced oxidative stress, DNA damage at telomeres and cell apoptosis besides decreased telomerase activity," (in eng), *Hum Mol Genet,* vol. 33, no. 9, pp. 818-834, Apr 18 2024.

[3] N. W. Kim *et al.*, "Specific association of human telomerase activity with immortal cells and cancer," (in eng), *Science,* vol. 266, no. 5193, pp. 2011-5, Dec 23 1994.

[4] D. Hockemeyer and K. Collins, "Control of telomerase action at human telomeres," (in eng), *Nat Struct Mol Biol,* vol. 22, no. 11, pp. 848-52, Nov 2015.

[5] S. Bajaj, M. S. Kumar, G. J. Peters, and Y. C. Mayur, "Targeting telomerase for its advent in cancer therapeutics," *Medicinal Research Reviews,* vol. 40, no. 5, pp. 1871-1919, 2020/09/01 2020.

[6] P. Fragkiadaki *et al.*, "Telomere length and telomerase activity in osteoporosis and osteoarthritis," (in eng), *Exp Ther Med,* vol. 19, no. 3, pp. 1626-1632, Mar 2020.

[7] E. Vasilopoulos *et al.*, "The association of female and male infertility with telomere length (Review)," (in eng), *Int J Mol Med,* vol. 44, no. 2, pp. 375-389, Aug 2019.

[8] C. Bryan, C. Rice, H. Hoffman, M. Harkisheimer, M. Sweeney, and E. Skordalakes, "Structural Basis of Telomerase Inhibition by the Highly Specific BIBR1532," (in eng), *Structure,* vol. 23, no. 10, pp. 1934-1942, Oct 6 2015.

[9] E. Pascolo *et al.*, "Mechanism of human telomerase inhibition by BIBR1532, a synthetic, non-nucleosidic drug candidate," (in eng), *J Biol Chem,* vol. 277, no. 18, pp. 15566-72, May 3 2002.

[10] H. El-Daly, M. Kull, S. Zimmermann, M. Pantic, C. F. Waller, and U. M. Martens, "Selective cytotoxicity and telomere damage in leukemia cells using the telomerase inhibitor BIBR1532," (in eng), *Blood,* vol. 105, no. 4, pp. 1742-9, Feb 15 2005.

[11] F. Doğan *et al.*, "Investigation of the effect of telomerase inhibitor BIBR1532 on breast cancer and breast cancer stem cells," (in eng), *J Cell Biochem,* vol. 120, no. 2, pp. 1282-1293, Feb 2019.

[12] D. K. Barma, A. Elayadi, J. R. Falck, and D. R. Corey, "Inhibition of telomerase by BIBR 1532 and related analogues," (in eng), *Bioorg Med Chem Lett,* vol. 13, no. 7, pp. 1333-6, Apr 7 2003.

[13] Y. Wu *et al.*, "Tumor-Oriented Telomerase-Terminated Nanoplatform as Versatile Strategy for Multidrug Resistance Reversal in Cancer Treatment," (in eng), *Adv Healthc Mater,* vol. 9, no. 7, p. e1901739, Apr 2020.

[14] A. N. Guterres and J. Villanueva, "Targeting telomerase for cancer therapy," (in eng), *Oncogene,* vol. 39, no. 36, pp. 5811-5824, Sep 2020.

[15] H. O. Tawfik *et al.*, "New Genetic Bomb Trigger: Design, Synthesis, Molecular Dynamics Simulation, and Biological Evaluation of Novel BIBR1532-Related Analogs Targeting Telomerase against Non-Small Cell Lung Cancer," (in eng), *Pharmaceuticals (Basel),* vol. 15, no. 4, p. 481, Apr 14 2022.

[16] C. Liu, H. Zhou, X. B. Sheng, X. H. Liu, and F. H. Chen, "Design, synthesis and SARs of novel telomerase inhibitors based on BIBR1532," *Bioorganic Chemistry,* vol. 102, p. 104077, 2020/09/01/ 2020.

[17] M. A. Read *et al.*, "Molecular modeling studies on G-quadruplex complexes of telomerase inhibitors: structure-activity relationships," (in eng), *J Med Chem,* vol. 42, no. 22, pp. 4538-46, Nov 4 1999.

[18] H. S. Huang *et al.*, "Synthesis, human telomerase inhibition and anti-proliferative studies of a series of 2,7-bis-substituted amido-anthraquinone derivatives," (in eng), *Bioorg Med Chem,* vol. 16, no. 14, pp. 6976-86, Jul 15 2008.

[19] K. R. Begnini *et al.*, "Apoptosis induction by 7-chloroquinoline-1,2,3-triazoyl carboxamides in triple negative breast cancer cells," *Biomedicine & Pharmacotherapy,* vol. 91, pp. 510-516, 2017/07/01/ 2017.

[20] L. Pietrovito, M. Iozzo, M. Bacci, E. Giannoni, and P. Chiarugi, "Treatment with Cannabinoids as a Promising Approach for Impairing Fibroblast Activation and Prostate Cancer Progression," (in eng), *Int J Mol Sci,* vol. 21, no. 3, p. 787, Jan 25 2020.

[21] H. Zhang, S. Li, Y. Si, and H. Xu, "Andrographolide and its derivatives: Current achievements and future perspectives," (in eng), *Eur J Med Chem,* vol. 224, p. 113710, Nov 15 2021.

[22] H. L. Soo, S. Y. Quah, I. Sulaiman, S. R. Sagineedu, J. C. W. Lim, and J. Stanslas, "Advances and challenges in developing andrographolide and its analogues as cancer therapeutic agents," *Drug Discovery Today,* vol. 24, no. 9, pp. 1890-1898, 2019/09/01/ 2019.

[23] J. Hu *et al.*, "The therapeutic potential of andrographolide in cancer treatment," (in eng), *Biomed Pharmacother,* vol. 180, p. 117438, Nov 2024.

[24] D. J. Newman and G. M. Cragg, "Natural products as sources of new drugs over the last 25 years," (in eng), *J Nat Prod,* vol. 70, no. 3, pp. 461-77, Mar 2007.

[25] A. G. Atanasov, S. B. Zotchev, V. M. Dirsch, and C. T. Supuran, "Natural products in drug discovery: advances and opportunities," (in eng), *Nat Rev Drug Discov,* vol. 20, no. 3, pp. 200-216, Mar 2021.

[26] R. Akter, A. C. Bishakha, R. Rajib, A. Raj, M. S. Roja, and F. Noor, "Targeting telomere dynamics with plant-derived compounds: Molecular strategies against aging," *Current Research in Pharmacology and Drug Discovery,* vol. 9, p. 100238, 2025/01/01/ 2025.

[27] F. Shirgahi Talari, K. Bagherzadeh, S. Golestanian, M. Jarstfer, and M. Amanlou, "Potent Human Telomerase Inhibitors: Molecular Dynamic Simulations, Multiple Pharmacophore-Based Virtual Screening, and Biochemical Assays," (in eng), *J Chem Inf Model,* vol. 55, no. 12, pp. 2596-610, Dec 28 2015.

[28] Z. F. Fan *et al.*, "Design, Synthesis and Molecular Docking Analysis of Flavonoid Derivatives as Potential Telomerase Inhibitors," (in eng), *Molecules,* vol. 24, no. 17, Sep 1 2019.

[29] J. D. Durrant and J. A. McCammon, "Molecular dynamics simulations and drug discovery," (in eng), *BMC Biol,* vol. 9, p. 71, Oct 28 2011.

[30] L. Zhao, Y. Zhu, J. Wang, N. Wen, C. Wang, and L. Cheng, "A brief review of protein-ligand interaction prediction," (in eng), *Comput Struct Biotechnol J,* vol. 20, pp. 2831-2838, 2022.

[31] R. Luo *et al.*, "Insights into Protein-Ligand Noncovalent Interaction Networks: A Database Survey and Quantum Chemistry Calculation Study," (in eng), *J Med Chem,* vol. 69, no. 6, pp. 6965-6975, Mar 26 2026.

[32] S. Genheden and U. Ryde, "The MM/PBSA and MM/GBSA methods to estimate ligand-binding affinities," (in eng), *Expert Opin Drug Discov,* vol. 10, no. 5, pp. 449-61, May 2015.

[33] E. Persch, O. Dumele, and F. Diederich, "Molecular Recognition in Chemical and Biological Systems," *Angewandte Chemie International Edition,* vol. 54, no. 11, pp. 3290-3327, 2015/03/09 2015.

[34] H. Wei and J. A. McCammon, "Structure and dynamics in drug discovery," *npj Drug Discovery,* vol. 1, no. 1, p. 1, 2024/11/07 2024.

[35] B. S. Zerbe, D. R. Hall, S. Vajda, A. Whitty, and D. Kozakov, "Relationship between hot spot residues and ligand binding hot spots in protein-protein interfaces," (in eng), *J Chem Inf Model,* vol. 52, no. 8, pp. 2236-44, Aug 27 2012.

[36] R. Friedman, "Resistance mutations, drug binding and drug residence times," *Current Opinion in Structural Biology,* vol. 95, p. 103158, 2025/12/01/ 2025.

[37] Z. Yang *et al.*, "A mutation-induced drug resistance database (MdrDB)," *Communications Chemistry,* vol. 6, no. 1, p. 123, 2023/06/14 2023.

[38] Q. K. Thai, P. Huynh, B. H. Nguyen, and N. P. Nguyen, "Structure-Based Identification Of Telomerase Inhibitors From *Andrographis Paniculata*," *International Journal of Drug Delivery Technology,* vol. 16, no. 6s, pp. 725-736, 2026.

[39] M. J. Abraham *et al.*, "GROMACS: High performance molecular simulations through multi-level parallelism from laptops to supercomputers," (in eng), *SoftwareX,* vol. 1, pp. 19-25, 2015.

[40] W. Humphrey, A. Dalke, and K. Schulten, "VMD: visual molecular dynamics," (in eng), *J Mol Graph,* vol. 14, no. 1, pp. 33-8, 27-8, Feb 1996.

[41] M. F. Adasme *et al.*, "PLIP 2021: expanding the scope of the protein–ligand interaction profiler to DNA and RNA," *Nucleic Acids Res,* vol. 49, no. W1, pp. W530-W534, Jul 2 2021.

[42] E. C. Meng *et al.*, "UCSF ChimeraX: Tools for structure building and analysis," (in eng), *Protein Sci,* vol. 32, no. 11, p. e4792, Nov 2023.

[43] M. S. Valdés-Tresanco, M. E. Valdés-Tresanco, P. A. Valiente, and E. Moreno, "gmx_MMPBSA: A New Tool to Perform End-State Free Energy Calculations with GROMACS," *Journal of Chemical Theory and Computation,* vol. 17, no. 10, pp. 6281-6291, 2021/10/12 2021.

[44] A. Grossfield, P. N. Patrone, D. R. Roe, A. J. Schultz, D. W. Siderius, and D. M. Zuckerman, "Best Practices for Quantification of Uncertainty and Sampling Quality in Molecular Simulations [Article v1.0]," (in eng), *Living J Comput Mol Sci,* vol. 1, no. 1, 2018.

[45] J. Yoo, C. Y. Li, S. M. Slone, C. Maffeo, and A. Aksimentiev, "A Practical Guide to Molecular Dynamics Simulations of DNA Origami Systems," (in eng), *Methods Mol Biol,* vol. 1811, pp. 209-229, 2018.

[46] L. J. Smith, X. Daura, and W. F. van Gunsteren, "Assessing equilibration and convergence in biomolecular simulations," (in eng), *Proteins,* vol. 48, no. 3, pp. 487-96, Aug 15 2002.

[47] Z. Yang, Y. Li, G. Zhou, X. Chen, D. Tao, and N. Hu, "Molecular Dynamics Simulations of Hydrogen Bond Dynamics and Far-Infrared Spectra of Hydration Water Molecules around the Mixed Monolayer-Protected Au Nanoparticle," *The Journal of Physical Chemistry C,* vol. 119, no. 4, pp. 1768-1781, 2015/01/29 2015.

[48] W. Swegat, J. Schlitter, P. Krüger, and A. Wollmer, "MD simulation of protein-ligand interaction: formation and dissociation of an insulin-phenol complex," (in eng), *Biophys J,* vol. 84, no. 3, pp. 1493-506, Mar 2003.

[49] Y. Fu, J. Zhao, and Z. Chen, "Insights into the Molecular Mechanisms of Protein-Ligand Interactions by Molecular Docking and Molecular Dynamics Simulation: A Case of Oligopeptide Binding Protein," *Computational and Mathematical Methods in Medicine,* vol. 2018, no. 1, p. 3502514, 2018/01/01 2018.

[50] G. A. Holdgate, T. D. Meek, and R. L. Grimley, "Mechanistic enzymology in drug discovery: a fresh perspective," *Nature Reviews Drug Discovery,* vol. 17, no. 2, pp. 115-132, 2018/02/01 2018.

[51] P. Tuffery and P. Derreumaux, "Flexibility and binding affinity in protein-ligand, protein-protein and multi-component protein interactions: limitations of current computational approaches," (in eng), *J R Soc Interface,* vol. 9, no. 66, pp. 20-33, Jan 7 2012.

[52] V. Mullapudi *et al.*, "Network of hotspot interactions cluster tau amyloid folds," *Nature Communications,* vol. 14, no. 1, p. 895, 2023/02/16 2023.

[53] D. Yehorova, B. Di Geronimo, M. Robinson, P. M. Kasson, and S. C. L. Kamerlin, "Using residue interaction networks to understand protein function and evolution and to engineer new proteins," *Current Opinion in Structural Biology,* vol. 89, p. 102922, 2024/12/01/ 2024.

[54] S. J. Fleishman, J. E. Corn, E. M. Strauch, T. A. Whitehead, J. Karanicolas, and D. Baker, "Hotspot-centric de novo design of protein binders," (in eng), *J Mol Biol,* vol. 413, no. 5, pp. 1047-62, Nov 11 2011.